Article

Poleward shift of subtropical highs drives Patagonian glacier mass loss

Brice Noël [1] ✉, Stef Lhermitte [2,3], Bert Wouters [3] & Xavier Fettweis [1]

Patagonian glaciers have been rapidly losing mass in the last two decades, but the driving processes remain poorly known. Here we use two state-of-the-art regional climate models to reconstruct long-term (1940-2023) glacier surface mass balance (SMB), i.e., the difference between precipitation accumulation, surface runoff and sublimation, at about 5 km spatial resolution, further statistically downscaled to 500 m. High-resolution SMB agrees well with in-situ observations and, combined with solid ice discharge estimates, captures recent GRACE/GRACE-FO satellite mass change. Glacier mass loss coincides with a long-term SMB decline (-0.35 Gt yr^{-2}), primarily driven by enhanced surface runoff ($+0.47$ Gt yr^{-2}) and steady precipitation. We link these trends to a poleward shift of the subtropical highs favouring warm northwesterly air advections towards Patagonia ($+0.14$°C dec^{-1} at 850 hPa). Since the 1940s, Patagonian glaciers have lost 1350 $\pm$ 449 Gt of ice, equivalent to 3.7 $\pm$ 1.2 mm of global mean sea-level rise.

Situated in the Southern Andes, Patagonia hosts the largest glacier area within the southern hemisphere, excluding the Antarctic ice sheet[1–3]. Besides small mountain glaciers, Patagonia encompasses three major icefields, namely the Northern (NPI; ~4000 km^2)[4] and Southern Patagonian Icefields (SPI; ~13,000 km^2)[5,6], and the Cordillera Darwin Icefield (CDI; ~2600 km^2)[7] located in the Tierra del Fuego archipelago (inset maps in Fig. 1a). Patagonian glaciers are on average 181 m thick[2], with a maximum of 1400 m in deep glacial valleys[3]. Altogether, these glaciers hold 4772 $\pm$ 1242 Gt of ice[8], eventually raising global sea level by ~13 mm if totally melted. Extrapolation of glaciological and geodetic observations suggests that Patagonia has experienced glacier mass loss since the early 1960s, contributing about 3.3 mm to global sea-level rise in the period 1961-2016[9]. The latest assessment from the Glacier Mass Balance Intercomparison Exercise (GlaMBIE)[8] reported rapid glacier mass loss of 26.5 $\pm$ 6.5 Gt yr^{-1} in the last two decades (2000-2023), equivalent to an average 0.07 mm sea-level rise each year. GlaMBIE estimates combine 13 mass change data sets including remote sensing (altimetry and gravimetry), geodetic and glaciological measurements. The three major icefields are responsible for 83% of the total mass loss[10], while the remainder is attributed to smaller neighbouring mountain glaciers. Storing only 3% of the Earth's total ice

volume outside polar ice sheets[2], Patagonia is disproportionately responsible for ~10% of the glacier contribution to sea-level rise (2002-2016)[11].

Mass change (MB) of Patagonian glaciers can be quantified by subtracting solid ice discharge (D), i.e., frontal ablation of calving icebergs, from the glacier surface mass balance (SMB), i.e., the difference between mass gained from precipitation accumulation and lost from meltwater runoff and sublimation. NPI and SPI icefields generally discharge ice into the ocean on the western side of the Andes, while they typically flow into proglacial lakes on the eastern side[1]. Remotely sensed solid ice discharge estimates indicate that NPI and SPI accounted for 15.1 $\pm$ 1.1 Gt yr^{-1} on average in 1968–1999[1], which further increased to 24.1 $\pm$ 1.7 Gt yr^{-1} in 2000–2019[12]. SPI glaciers contributed about 80% to the total solid ice discharge flux in 1968–1999[1], and up to 90% in 2000-2019[12]. While remaining steady across most SPI glacier calving fronts, solid ice discharge has however experienced an overall decreasing trend since the 2000s, dominated by the continuous advance of a single glacier, namely Pio XI South[12]. This decreasing trend reveals that declining glacier SMB has been playing an increasing role in the recent Patagonian glacier mass loss[13], which is expected to further accelerate in the future[14,15]. Previous NPI and SPI SMB

[1]Laboratory of Climatology, Department of Geography, SPHERES research unit, University of Liège, Liège, Belgium. [2]Department of Earth & Environmental Sciences, KU Leuven, Leuven, Belgium. [3]Department of Geoscience & Remote Sensing, Delft University of Technology, Delft, Netherlands. ✉e-mail: bnoel@uliege.be
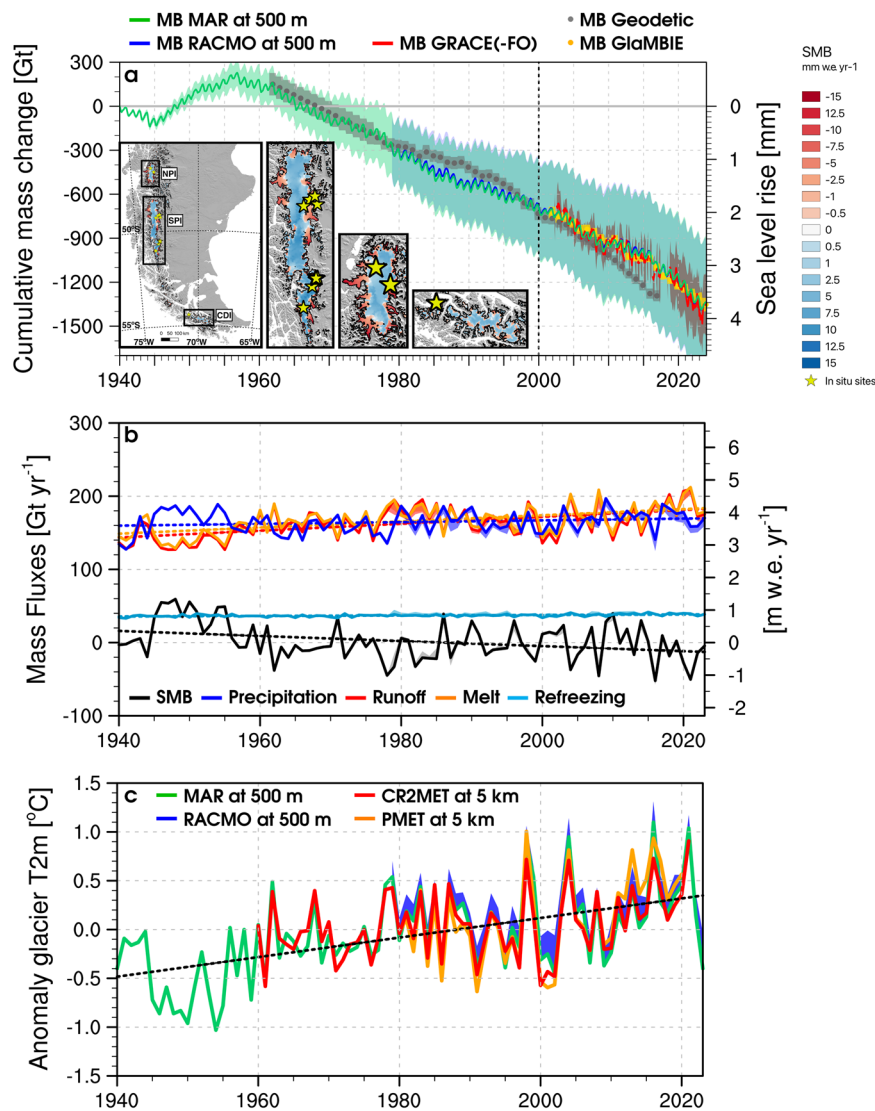
Fig. 1 | Long-term mass loss of Patagonian glaciers. a Monthly cumulative mass change (MB = SMB - D) of Patagonian glaciers. Mass change is estimated as the difference between downscaled surface mass balance (SMB) from MAR (green line, 1940-2023) and RACMO (blue line, 1979-2023) at 500 m resolution, and solid ice discharge estimates (D) from 1968-1999[1] and 2000–2019[12], assuming that these remain valid pre-1968 (1940–1999) and post-2019 (2000-2023), respectively. The vertical dashed line marks the transition between these two solid ice discharge products. Geodetic mass change from Zemp et al. (2019)[9] (1961–2016), GRACE/ GRACE-FO satellite mass change (2002–2023), and from the latest GlaMBIE assessment (2000–2023)[8] are shown in grey, red and orange respectively. Coloured bands represent uncertainties. Inset maps show averaged MAR SMB at 500 m (1940–2023) with a zoom in on three major Patagonian icefields: Northern

(NPI) and Southern Patagonian Icefield (SPI), and Cordillera Darwin Icefield (CDI). The background hillshade is derived from the Shuttle Radar Topography Mission (SRTM)[30] digital elevation model (DEM) down-sampled to 250 m spatial resolution. Mass change is converted to global sea-level rise equivalent assuming that 362.5 Gt of ice raises sea-level by 1 mm[75]. **b** Annual mean SMB components from MAR (coloured solid lines) and RACMO (coloured bands) at 500 m. **c** Annual mean 2 m air temperature anomaly (relative to 1960–1989), spatially averaged over glacier-covered grid-cells (i.e., ice fraction> 0) from MAR (green line) and RACMO (blue band) at 500 m, from CR2MET (red line, 1960–2021)[32] and PMET (orange line, 1980–2020)[31] meteorological grids at 5 km. In **b**–**c**, long-term trends are derived from MAR (dashed lines).

reconstructions using positive degree day (PDD)[16], regional climate models[17], sometimes downscaled using fixed lapse rates to force sim-plified mass balance models[13,18,19] (Methods), e.g., neglecting rain and meltwater retention in snow, suggested a positive but insignificant SMB trend in the period 1975-2015. This trend was ascribed to long-term snowfall increase combined with meltwater runoff decline. However, these results remain highly uncertain since low-resolution climate models are prone to overestimate precipitation over the steep Andes[20], while they cannot accurately capture high meltwater runoff rates across narrow glaciers[17]. Furthermore, a positive SMB trend contradicts the recent mass loss increase observed in the last two decades[10,21–25], highlighting large uncertainties in modelled SMB and a poor understanding of mass change drivers.

Here we use two state-of-the-art regional climate models, namely MAR version 3.14 (1940-2023) and RACMO version 2.3p2 (1979-2023)[17,26], to reconstruct the contemporary SMB of Patagonian glaciers at 5 km and 5.5 km spatial resolution, respectively (Supplementary Fig. 1) (Methods). Both models are forced by the latest ERA5 climate reanalysis[27] and statis-tically downscaled to a 500 m grid[28,29] (Methods). In brief, statistical downscaling uses daily, local vertical gradients to correct SMB and com-ponents, i.e., total precipitation, snowfall, total sublimation, total melt and subsequent runoff, for elevation difference between the low-resolution surface topography prescribed in both models, and the high-resolution Shuttle Radar Topography Mission (SRTM) digital elevation model (DEM) version 4[30] at 30 m resolution, down-sampled to a 500 m grid (Supple-mentary Fig. 2). Moderate Resolution Imaging Spectroradiometer
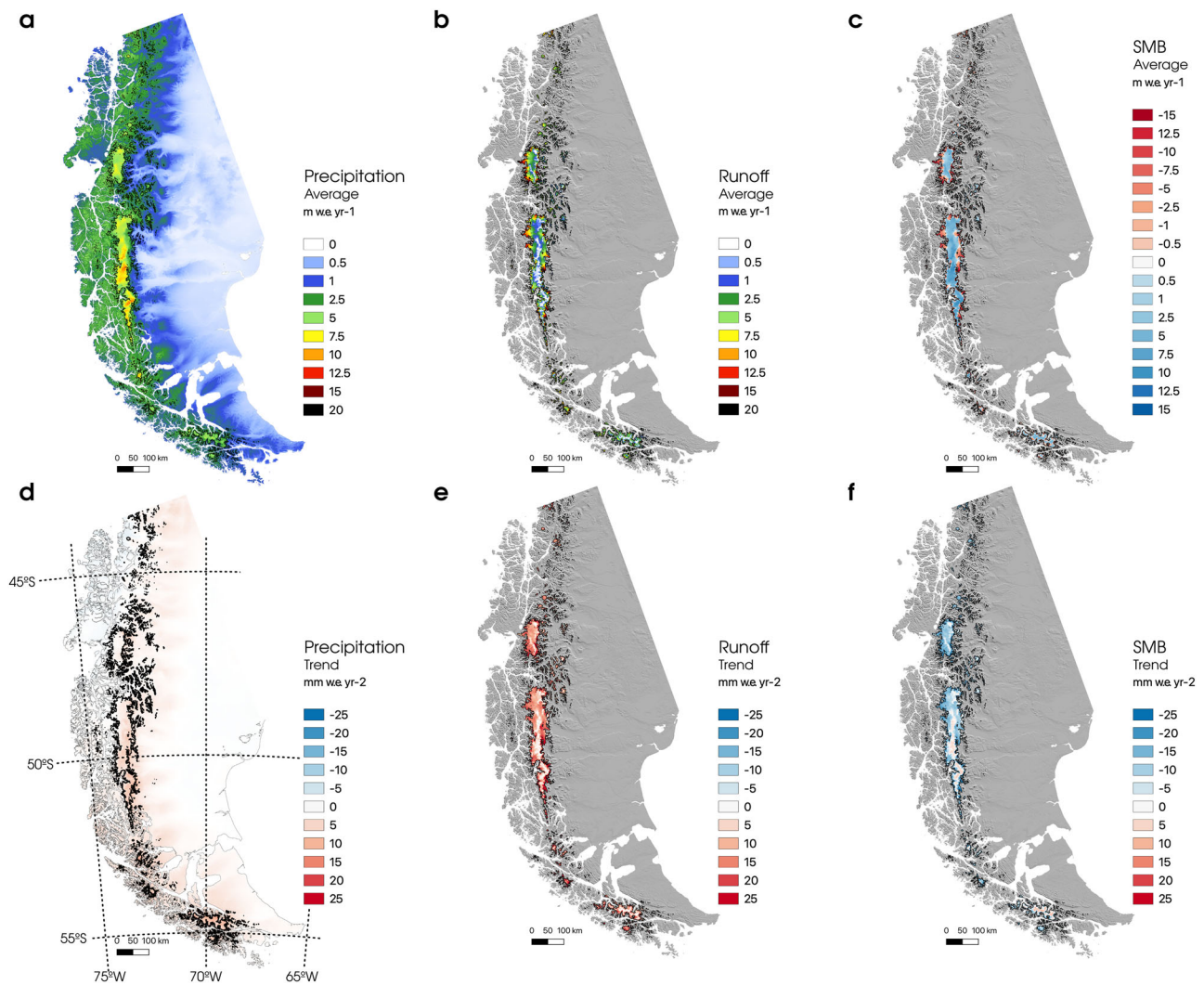
Fig. 2 | Long-term surface mass balance components and spatial trends. Long-term average of (**a**) total precipitation, (**b**) surface runoff and (**c**) surface mass balance (SMB) as modelled by MAR, statistically downscaled to 500 m, for the period 1940-2023. **d–f** same as **a–c** but for long-term trends (1940-2023). The background hillshade is derived from the Shuttle Radar Topography Mission (SRTM)[30] digital elevation model (DEM) down-sampled to 250 m spatial resolution.

(MODIS) albedo records at 500 m resolution are further used to correct surface melt and runoff for the albedo of exposed dark bare ice in summer. In line with previous studies[17,20], RACMO strongly overestimates orographic-forced precipitation across the steep Andes. The statistically downscaled RACMO total precipitation is therefore adjusted and reduced by 36.5% over ice-covered grid-cells on a daily basis (Methods). This approach ensures that the precipitation adjustment has a dominating effect in regions where overestimates peak, notably across the steep and moist windside flank of the Andes, i.e., accumulation > 15 m water equivalent (w.e.) (Supplementary Fig. S1b). The justification for this adjustment is to eliminate the large positive bias relative to mass change records from the Gravity Recovery and Climate Experiment (GRACE) and Follow-On (GRACE-FO) missions[24] (Supplementary Fig. 4b, c), when combined with solid ice discharge[1,12]. Such adjustment is not required for the statistically downscaled MAR product (Supplementary Fig. S4b). Hereafter, we use the high-resolution original MAR and precipitation-adjusted RACMO downscaled SMB products to identify the drivers of Patagonian glacier mass loss, and estimate their contribution to global sea-level rise.

Results

Mass change of Patagonian glaciers

Figure 1a shows long-term Patagonian glacier monthly cumulative mass change (MB = SMB - D) derived from MAR (green line; 1940-2023)

and RACMO SMB (blue line; 1979-2023), further statistically downscaled to 500 m (Fig. 2c and Supplementary Fig. 3c), combined with published solid ice discharge estimates[1,12]. Since published estimates do not fully cover the period 1940-2023, we assume that the long-term solid ice discharge averages for 1968–1999[1] and 2000-2019[12] remain valid prior 1968 and post 2019, respectively. Therefore, we set solid ice discharge to 15.1 ± 1.1 Gt yr^{-1} in 1940-1999[1], with a step increase to 24.1 ± 1.7 Gt yr^{-1} in 2000−2023[12]. Note that these published solid ice discharge estimates, i.e., annual averages for two periods, may not fully capture interannual and seasonal variabilities within their uncertainty range. Since 1940, Patagonian glaciers have been experiencing sustained mass loss (MB < 0), though briefly interrupted by a short mass gain episode (MB > 0) in the period 1945−1955 (Fig. 1a). This long-term negative trend is in line with geodetic mass change records spanning 1961−2016 (grey dots)[9], with averaged observed and modelled mass loss of 26.2 ± 11.0 Gt yr^{-1} (Geodetic)[9] and 22.3 ± 5.4 Gt yr^{-1} (MAR), respectively. Modelled mass loss from MAR (28.8 ± 5.4 Gt yr^{-1}) and RACMO (29.9 ± 5.4 Gt yr^{-1}) aligns well with GRACE/GRACE-FO satellite measurements (27.8 ± 11.0 Gt yr^{-1}) (red line) in the last two decades (2002−2023), showing both a strong correlation (R^2 = 0.98) and a low RMSE (~ 35 Gt) for both models (Supplementary Fig. 4c). Furthermore, our estimates are in excellent agreement with previously published mass change records including the latest GlaMBIE assessment[8]

(Supplementary Table 2), that reports mass loss of 26.5 ± 6.5 Gt yr^{-1} in 2000–2023 (orange dots) compared to 27.3 ± 5.4 Gt yr^{-1} in MAR and 28.5 ± 5.4 Gt yr^{-1} in RACMO, respectively. Using our two high-resolution products, we estimate that Patagonian glaciers have lost 1350 ± 499 Gt of ice since 1940, contributing 3.7 ± 1.2 mm to global sea-level rise.

Long-term surface mass balance trends

To explore the role of surface processes in the long-term mass loss, Fig. 1b shows annual cumulative SMB and components from both MAR (solid lines; 1940-2023) and adjusted RACMO models (bands; 1979-2023), statistically downscaled to 500 m (Fig. 2a–c and Supplementary Fig. 3a–c). For SMB evaluation, we use 74 stake measurements (1980-2019) collected at 38 in-situ sites across NPI (2 sites), SPI (26 sites), and CDI (19 sites) (yellow stars in the inset maps of Fig. 1a) (Methods). MAR and RACMO agree well with observations, i.e., R^2 reaches 0.83 and 0.74, and RMSE ranges from 3.3 to 4.9 m w.e. respectively (Supplementary Fig. 5b, e). Cross-model comparison between each SMB component in the overlapping period 1979-2023 shows good agreement, with high correlation ($0.92 \le R^2 \le 0.94$) and overall small model differences (1 to 7%) (Supplementary Fig. 6a–e) (Methods). Although glacier-integrated differences are small, low correlation ($R^2 = 0.32$) is found for modelled retention and refreezing in firn (Supplementary Fig. 6f), i.e., the perennial compressed snow layer covering the glacier accumulation areas (SMB > 0 in the inset maps of Fig. 1a). We attribute these discrepancies to the different snow modules incorporated in MAR and RACMO (Methods). Supplementary Fig. 3d–f shows spatial differences between downscaled SMB components from MAR and RACMO at 500 m. Total precipitation shows large-scale spatial differences between the two models, i.e., with lower values in MAR on the western windside slope, and higher values on the eastern leeside (Supplementary Fig. 3d). This indicates a more pronounced foehn effect on the Patagonian Andes from prevailing westerly winds in RACMO, while MAR distributes precipitation more uniformly (Fig. 2a). This results in total precipitation being 8.0 Gt larger in MAR than in adjusted RACMO (Supplementary Fig. 6b, c and Supplementary Table 1). In addition, MAR has higher runoff than RACMO (5.6 Gt yr^{-1} in Supplementary Fig. 6d and Supplementary Table 1), notably across small mountain glaciers and at the icefields margins (Supplementary Fig. 3e). This results from both higher meltwater production (1.7 Gt yr^{-1} in Supplementary Fig. 6e) and rainfall in MAR (1.3 Gt yr^{-1} in Supplementary Fig. 6c), combined with lower refreezing in firn (2.6 Gt yr^{-1} in Supplementary Fig. 6f). Although having a small contribution to SMB, we find that total sublimation is overall 2.1 Gt lower in MAR than in RACMO (Supplementary Table 1). Consequently, glacier-integrated SMB is almost equal in both models (0.3 Gt yr^{-1} difference in Supplementary Fig. 6a), and spatial differences are mostly driven by precipitation distribution patterns (Supplementary Fig. 3f). To ensure reliable surface accumulation, we compare modelled glacier-integrated total precipitation with corresponding estimates from the gridded meteorological PMET data set at 5 km spatial resolution (1980–2020)[31] (Supplementary Fig. 7). We find excellent model agreement ($R^2 = 0.86$ and 0.91) with low RMSE of 8.7 Gt yr^{-1} and 14.0 Gt yr^{-1}, i.e., equivalent to 5% and 8% of the PMET total precipitation, in MAR and RACMO respectively.

Using long-term MAR timeseries (Fig. 1b), we find that Patagonian glacier SMB (Fig. 2c) remained close to equilibrium at 1.6 ± 0.3 Gt yr^{-1} on average (1940-2023), the result of total precipitation (164.7 ± 8.0 Gt yr^{-1}) (Fig. 2a), i.e., partitioned in snowfall (79%) and rainfall (21%), approximately balancing surface runoff (163.0 ± 5.6 Gt yr^{-1}) (Fig. 2b) (Supplementary Table 1). At the same time, SMB experiences large interannual variability (SD = 25.7 Gt yr^{-1}), primarily driven by runoff fluctuations (SD = 21.1 Gt yr^{-1}) being 40% larger than those of total precipitation (SD = 15.2 Gt yr^{-1}). Large interannual variability is illustrated by peak high and low SMB reaching +59.4 Gt in year 1948, and

-52.2 Gt in year 2016 (Fig. 1b). In these years, SMB is two to three-folds larger than the corresponding solid ice discharge flux (D = 15.1 to 24.1 Gt)[1,12], indicating that SMB fluctuations primarily drive the variability and trend of Patagonian glacial mass change. In the period 1940–2023, we find that Patagonian glaciers have undergone sustained, and significant SMB decline (-0.35 ± 0.23 Gt yr^{-2}, p < 0.01) (Fig. 1b). Our product suggests that long-term SMB decline is driven by insignificant total precipitation increase (0.12 ± 0.13 Gt yr^{-2}, p > 0.05) notably in the glacier interior accumulation zones (Fig. 2d), combined with significantly enhanced surface runoff (0.47 ± 0.16 Gt yr^{-2}, *p* < 0.01) across low-lying glacier ablation zones (Fig. 2e). Interestingly, the insignificant precipitation trend stems from steady snowfall accumulation (0.03 ± 0.12 Gt yr^{-2}, *p* > 0.05) with significant rainfall increase (0.09 ± 0.03 Gt yr^{-2}, *p* < 0.01). The increase in runoff coincides with a significant rise in annual mean glacier near-surface air temperature (T2m) (0.10 ± 0.03°C dec^{-1}, *p* < 0.01), hence triggering enhanced meltwater production (0.42 ± 0.14 Gt yr^{-2}, *p* < 0.01). Atmospheric warming is in line with two gridded meteorological data sets at 5 km spatial resolution, namely CR2MET (1960-2021)[32] and PMET (1980-2020)[31] (Fig. 1c). We conclude that, following long-term atmospheric warming (1940-2023), enhanced runoff at the glacier margins (Fig. 2e) exceeds the small precipitation increase inland (Fig. 2d), in turn significantly reducing SMB (Fig. 2f).

Drivers of long-term runoff increase

Patagonian glacier SMB strongly correlates with surface runoff in both MAR and RACMO (r = 0.80) (Fig. 3a), while the signal is much weaker for total precipitation (r = 0.61) (Fig. 3b). Our products thus indicate that long-term Patagonian glacier SMB responds predominantly to runoff rather than precipitation changes (Fig. 2d–f). At the same time, runoff is highly sensitive to glacier near-surface temperature anomalies with respect to 1960-1989 (r = 0.81) (Fig. 3c), indicating that long-term atmospheric warming triggers runoff increase. To investigate the link between atmospheric warming and runoff, Fig. 4a–c shows long-term ablation zone extent (SMB < 0) as a fraction of the total glacier area; the fraction of total precipitation falling as rain; and the glacier refreezing capacity, i.e., the fraction of rain and meltwater effectively retained or refrozen within the firn layer. The latter three quantities are first correlated to near-surface temperature anomalies (Fig. 4d–f) and then to surface runoff (Fig. 4g–i). MAR and RACMO agree well in the overlapping period 1979-2023, with strong correlation and small model differences for the ablation zone extent ($R^2 = 0.83$, difference = -2.4%), rainfall fraction ($R^2 = 0.96$, difference = -0.2%), and firn refreezing capacity ($R^2 = 0.70$, difference = -0.8%) (Fig. 4a–c).

Using long-term MAR timeseries, we find that the glacier ablation zones have significantly expanded since 1940 (+0.9 ± 0.5% dec^{-1}, *p* < 0.01), following near-surface atmospheric warming (r = 0.70, Fig. 4d). This stems from a significant long-term increase of the equilibrium line altitude (ELA, SMB = 0) by 8.9 ± 5.5 m dec^{-1} (*p* < 0.01). As a result, the ELA migrated upward from ~1220 m a.s.l. to ~1300 m a.s.l. between 1940 and 2023, further expanding the ablation zone area. This is further supported by the fact that MAR captures, within uncertainties, the ELA of NPI and SPI derived from previous observational and model estimates (Supplementary Table 3). Ablation zone expansion triggers runoff increase (r = 0.78, Fig. 4g) as enhanced melt eventually drains on top of impermeable bare ice exposed at the surface in summer. Furthermore, the contribution of rainfall to total precipitation has significantly increased (+0.4 ± 0.2% dec^{-1}, *p* < 0.01), the result of atmospheric warming favouring precipitation in the liquid phase (r = 0.67, Fig. 4e), which preferentially runs off on top of bare ice surfaces (r = 0.84, Fig. 4h). In the interior accumulation zone, firn retains roughly 18% of surface melt and rain in its pore space on average (1940-2023). Since 1940, firn refreezing capacity has significantly declined (−0.3 ± 0.1% dec^{-1}, *p* < 0.01) (Fig. 4c) following atmospheric warming
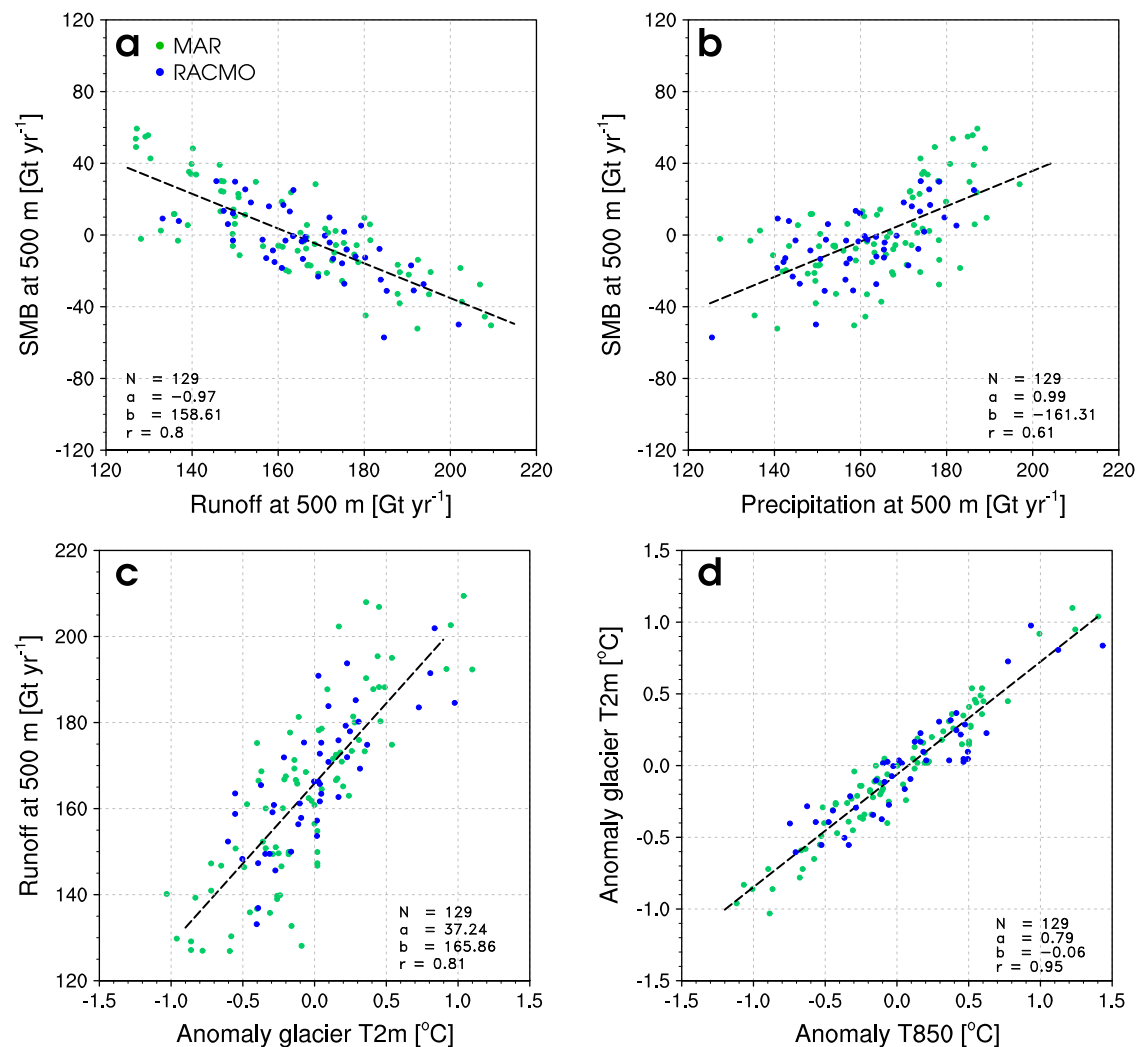
Fig. 3 | Surface mass balance response to atmospheric temperature anomalies. Correlation between (**a**) surface mass balance (SMB) and surface runoff, (**b**) SMB and total precipitation, (**c**) surface runoff and anomalies in glacier near-surface temperature (T2m), (**d**) anomalies in near-surface temperature and anomalies in 850 hPa atmospheric temperature (T850). Anomalies are estimated relative to the 1960-1989 period. MAR and RACMO data at 500 m are shown as blue and green dots respectively. For T2m, model data at 500 m are spatially averaged over glacier-covered grid-cells. Linear regression and relevant statistics, i.e., number of records (N), slope (a), intercept (b), and correlation (r), include both MAR (84 years) and RACMO (45 years) data sets. T850 data are retrieved from ERA5 reanalysis[27] within the yellow contour extracted for MAR and RACMO in Supplementary Fig. 8a, c, respectively. The MAR-derived yellow contour is also displayed in Fig. 5a, b.

(r = 0.70, Fig. 4f). This results in increased surface runoff across the glacier interior accumulation zone (r = 0.86, Fig. 4i) through i) the progressive removal of the firn layer, ii) a reduced firn replenishment as rainfall increases at the expense of snowfall, and iii) the depletion of available firn pore space following enhanced surface melt and rain storage. Through these combined processes, near-surface atmospheric warming drives enhanced surface runoff not only in low-lying ablation zones, but also, though to a smaller degree, in the higher interior accumulation zones (Fig. 2e).

Poleward shift of subtropical highs drives glacier mass loss
Atmospheric warming strongly correlates throughout the air column from the near-surface (T2m) up to the 850 hPa level (T850) (r = 0.95) (Fig. 3d), suggesting a large-scale circulation change origin besides the effect of global warming. Figure 5a shows long-term spatial correlation between T850 derived from the ERA5 reanalysis[27] and glacier-integrated surface runoff from MAR at 500 m (1940-2023). Strong links are generally found across the South Pacific and Atlantic Oceans, notably nearby the Southern Andes (r > 0.75, yellow contour in Fig. 5a and Supplementary Fig. 8a). Similar patterns hold for RACMO glacier

runoff in the period 1979-2023 (Supplementary Fig. 8c). To explore the drivers of this atmospheric warming, Fig. 5b maps long-term trends in T850 (°C dec⁻¹; background colour), geopotential height Z850 (m dec⁻¹; grey contours), and wind speed and direction (arrows) derived from ERA5 in 1940-2023. The Southern Pacific Subtropical Gyre, i.e., also called Saint Helena High (SHH in Fig. 5b; 30–45°S/130–160°W) experiences enhanced Z850 (> 2.5 m dec⁻¹), indicating a long-term strengthening. This is supported by stronger anticlockwise atmospheric circulation, and associated synoptic warming through enhanced air subsidence (> 0.2 °C dec⁻¹). Superimposed on this, the SHH has undergone a long-term poleward shift since 1940, highlighted by a pronounced southeastward curvature of the geopotential contours (80-110°W). Patagonian glaciers experience increased atmospheric pressure (1.01 ± 0.81 m dec⁻¹, p < 0.05) (Fig. 5c) that drives enhanced northwesterly warm subtropical air advection (Fig. 5b). This triggers significant atmospheric warming near the Southern Andes (0.14 ± 0.03 °C dec⁻¹, p < 0.01) (Fig. 5d), that is 17% larger than the global average (0.12 ± 0.01 °C dec⁻¹, p < 0.01). We conclude that this atmospheric warming is primarily responsible for the long-term runoff increase (r = 0.83) (Fig. 5d).
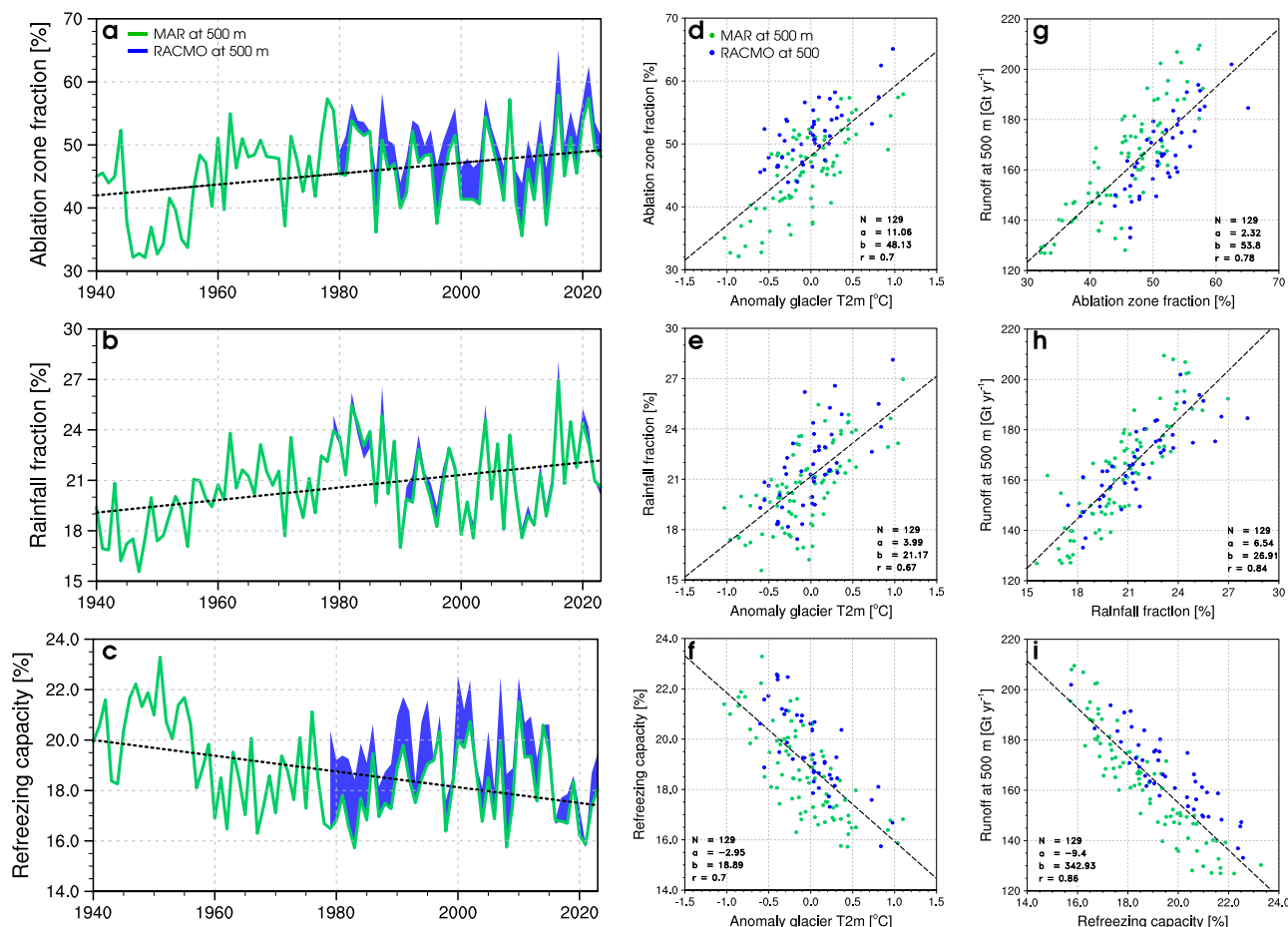
Fig. 4 | Long-term trends in surface processes affecting glacier runoff. Time series of annual (**a**) ablation zone fraction (%), i.e., relative to the total glacier area, (**b**) rainfall fraction (%), i.e., relative to the glacier-integrated total precipitation, (**c**) firn refreezing capacity (%), i.e., the fraction of total melt and rainfall retained or refrozen in firn, for the period 1940–2023. MAR and RACMO data at 500 m are shown as green lines and blue bands, respectively. Long-term trends (1940-2023) derived from MAR are shown as dashed lines. Correlation between anomalies in glacier near-surface temperature (T2m, relative to 1960–1989) and (**d**) ablation zone fraction, (**e**) rainfall fraction, and (**f**) firn refreezing capacity from MAR (green dots) and RACMO (blue dots) at 500 m. (**g–i**) same as (**d–e**) but correlated to surface runoff. In (**d–i**) linear regression and relevant statistics, i.e., number of records (N), slope (a), intercept (b), and correlation (r), include both MAR (84 years) and RACMO (45 years) data sets.

Discussion

Carrasco-Escaff et al. (2023)[13] previously explored the SMB response of Patagonian glaciers to climatic controls in the period 1980-2015. Opposite to our results, they found that the interannual variability and trends of glacier SMB were predominantly driven by precipitation (r = 0.87), rather than runoff fluctuations (r = -0.69). High accumulation years coincide with the formation of an anomalous low pressure system in the Drake Passage (DP in Fig. 5b and Supplementary Fig. 8b, d), i.e., situated to the south of Cape Horn, in turn favouring stronger westerlies and associated precipitation across Patagonian icefields. We find similar strong correlation between total precipitation and Z850 nearby the Drake Passage in both MAR (1940-2023) and RACMO (1979-2023) (Supplementary Fig. 8b, d). However, our results identify atmospheric warming and subsequent runoff increase as the prime control on SMB fluctuations and trends (r = -0.80 in Fig. 3a), while precipitation only plays a secondary role (r = 0.61 in Fig. 3b). This is further supported by the fact that the long-term SMB decline is driven by sustained runoff increase, with steady precipitation (Fig. 1b). This contrast to previous work is ascribed to the fact that our (adjusted) high-resolution data sets i) do not significantly overestimate precipitation across Patagonian Andes compared to gridded observations[20] (Supplementary Fig. 7a), and ii) do not significantly underestimate runoff in low-lying ablation zones relative to in-situ

measurements[17] (Supplementary Fig. 5b, e). This is further demonstrated by the good agreement between our downscaled mass change estimates from both MAR and RACMO, and recent geodetic, glaciological, and remote sensing records (Fig. 1a and Supplementary Table 2). Climate projections across NPI and SPI under a low (RCP2.6) and a high-end emission scenario (RCP8.5) by 2050[15] corroborate that the contemporary and future SMB variability and trends currently are, and will remain to be, primarily driven by atmospheric warming and runoff increase.

We ascribe long-term runoff increase to a poleward shift of subtropical high pressure systems, which has been observed in the southern hemisphere in the past four decades with latitudinal displacements ranging from 0.04 to 0.10° per decade[33]. The shift of high pressure gyres result from a positive feedback between anomalous rise in sea surface temperature and change in atmospheric circulation[34]. Subtropical sea surface temperature increase is attributed to anomalous Ekman pumping that strengthens surface convergence, hence transporting more heat from the Equator and further expanding the tropical warm water zone southward. Oceanic warming, in turn affects the atmospheric circulation by enhancing the subtropical high pressure systems, i.e., with stronger anticlockwise wind patterns that reinforce the Ekman pumping[34]. Poleward shift of warm subtropical waters strengthens high pressure gyres while displacing them
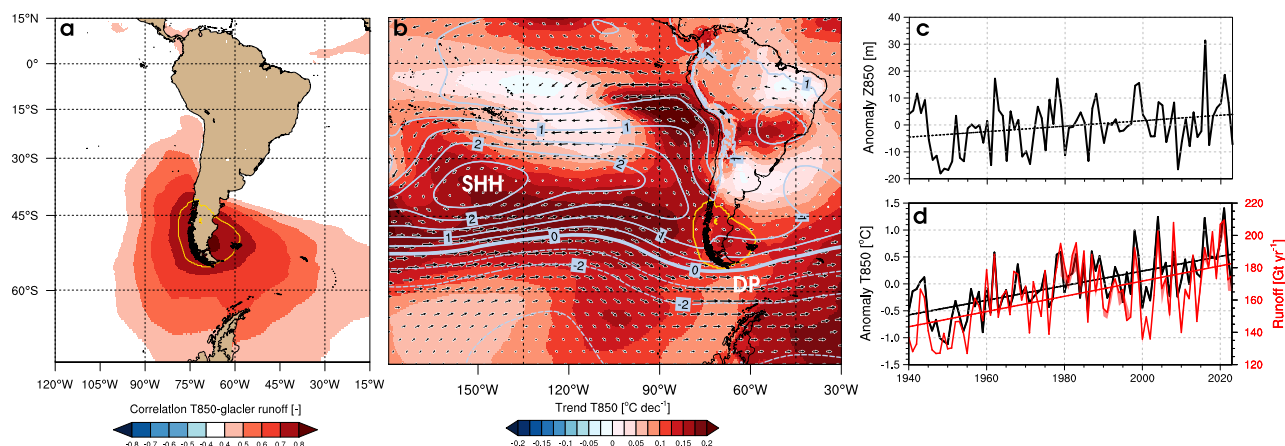
Fig. 5 | Poleward shift of subtropical highs enhances surface runoff. a Spatial correlation between glacier-integrated runoff from MAR at 500 m and 850 hPa atmospheric temperature (T850) from ERA5 reanalysis (1940-2023). The yellow contour highlights correlation r > 0.75 in MAR. **b** Spatial trends in T850 (background map), 850 hPa geopotential height (Z850, m dec⁻¹) (grey contour), and wind direction (arrows). The location of the Saint Helena High (SHH) and Drake Passage (DP) are also shown. **c** Timeseries of Z850 anomalies relative to 1960–1989 derived from ERA5 reanalysis (1940-2023) and extracted from a relevant region that encompasses the whole of Patagonia (yellow outline in **a**–**b**). **d** Timeseries of T850 anomalies relative to 1960–1989 derived from ERA5 reanalysis (solid black line; 1940-2023) and retrieved from the yellow contour extracted for MAR and RACMO in Supplementary Fig. 8a, c, respectively. MAR (solid red line; 1940–2023) and RACMO (red band; 1979-2023) runoff timeseries at 500 m are also shown.

southward, as reported e.g., for the SHH region in previous studies[34–36]. The drivers of this large-scale ocean-atmosphere interaction remain uncertain but are likely linked to global warming[33], and the SHH poleward shift is thus expected to continue in the future[33]. Here we link the SHH poleward shift, and associated northwesterly warm subtropical air advection, to a long-term surface runoff increase in Patagonia (1940–2023), hence driving enhanced glacier mass loss (Fig. 5d). Climate warming projections predict that mass loss of Patagonian icefields will persist in the future, raising global sea-level by 3.1 mm (RCP2.6) to 3.8 mm (RCP8.5) in the period 2012-2050, further reducing the remaining ice volume by 22% to 27% respectively[15]. At the current rate of mass loss, i.e., 24.2 ± 5.4 Gt yr⁻¹ in MAR and 24.5 ± 5.4 Gt yr⁻¹ in RACMO for 1979-2023 (Fig. 1a), Patagonian glaciers could completely melt away within the next 220 years. These estimates should be interpreted as conservative since none of MAR, RACMO, or the statistical downscaling procedure account for glacier retreat and thinning, nor for the evolution of calving processes.

Methods

Surface mass balance and mass change records

For SMB evaluation, we use 74 stake measurements spanning the period 1980-2019, and collected at 38 locations across NPI (2 sites), SPI (26 sites) and CDI (19 sites) (inset maps in Fig. 1a). SMB records were estimated from stakes and firn cores drilled on: i) San Rafael (1984)[37] and Nef (1996)[38] glaciers in NPI; ii) Perito Moreno (1980–1985[39] and 1996-2001[40,41]), De Los Tres (1995-1996)[42], Chico (1994–2001)[43], Cerro Gorra Blanca (1995–2001)[44,45], Tyndall (1998–2000)[46], and Pio XI (2000–2006)[45] glaciers in SPI; and iii) Monte Sarmiento Massif (2013-2019)[47] in CDI. We discarded data compiling less than 3 months of monitoring. For a meaningful comparison, we cumulated downscaled SMB at 500 m from MAR and RACMO over the overlapping months of measurements (Supplementary Fig. 5).

We compare monthly GRACE and GRACE-FO mass change records (and uncertainties)[24] for the period 2002-2023 with input-output method estimates (MB = SMB - D) (Fig. 1a and Supplementary Fig. 4). Annual mean solid ice discharge (D) was set to 15.1 ± 1.1 Gt yr⁻¹ in 1940-1999[1] and 24.1 ± 1.7 Gt yr⁻¹ in 2000–2023[12,48], assuming that these long-term estimates for 1968–1999 and 2000–2019 remain valid pre-1968 and post-2019 respectively, and were equally distributed within each month of the year. In future work, these solid ice discharge estimates

could be improved by exploiting historical imagery to cover the pre-satellite era[49], hence capturing potentially large long-term variability. Monthly SMB is derived from MAR and RACMO spatially integrated over glacier-covered grid-cells, i.e., ignoring seasonal snow and melt outside glaciers. While this may affect the amplitude of mass change, i.e., with peak snow/melt in winter/summer, it does not affect its trend since snow cannot accumulate outside glacier areas over the years.

Gridded meteorological records

We use two gridded meteorological data sets at 5 km, i.e., CR2MET (1960-2021)[32] and PMET (1980-2020)[31], to evaluate downscaled glacier-integrated total precipitation and snowfall from MAR and RACMO at 500 m spatial resolution (Supplementary Fig. 7). While the meteorological data sets correlate well in the overlapping period 1980-2020 ($R^2 = 0.71$), total precipitation is on average 32% (55.8 Gt yr⁻¹) larger in PMET than in CR2MET. Total precipitation in MAR and RACMO show excellent agreement with PMET ($R^2 = 0.86$ and 0.91; RMSE = 8.7 Gt yr⁻¹ and 14.0 Gt yr⁻¹ respectively), while being 44% to 37% larger than in CR2MET (51.6 Gt yr⁻¹ and 45.4 Gt yr⁻¹ respectively). We attribute the difference between the two meteorological data sets to the fact that CR2MET may only capture solid precipitation. This is supported by the relatively low RMSE obtained when comparing downscaled snowfall from MAR (15.3 Gt yr⁻¹) and RACMO (10.6 Gt yr⁻¹) to the CR2MET data set, i.e., 13% and 9% of the total precipitation in CR2MET, respectively.

We also compare anomalies in annual mean near-surface air temperature (T2m), spatially averaged over glacier-covered grid-cells, from MAR and RACMO with those of CR2MET (1960-2021) and PMET (1980–2020). For a meaningful comparison, anomalies are estimated with respect to the period 1960–1989, or the overlapping period in each data set, i.e., 1979–1989 for RACMO and 1980–1989 for PMET (Fig. 1c). All four data sets show excellent agreement with $0.74 < R^2 < 0.89$, and 0.14 °C < RMSE < 0.28 °C.

MAR: modèle atmosphérique régional

The Modèle Atmosphérique Régional version 3.14 (MARv3.14) implements the dynamical core developed by Gallée and Schayes (1994)[50] and the physics discussed by Fettweis et al. (2005)[51]. MAR has been used and thoroughly evaluated for glaciated areas, including the Greenland ice sheet[52], glaciers and ice caps of the Arctic region[53], and the Antarctic ice sheet[54]. The model incorporates a dedicated Soil Ice

Snow Vegetation Atmosphere Transfer (SISVAT) module[55] that is specifically adapted for snow and ice processes[56,57]. Surface melt, percolation and retention in firn, and subsequent surface runoff are simulated in a 21-layer snowpack. Snow albedo is computed in the CROCUS sub-module[58] based on snow grain properties (size, sphericity, dendricity), snow densification, solar zenith angle, cloud optical thickness, and surface meltwater ponding. Here, MAR is run at 5 km spatial resolution and forced at its lateral (seven pixels) and upper (stratosphere) atmospheric boundaries by the latest ERA5 climate reanalysis[27] (1940-2023). Forcing fields include temperature, pressure, specific humidity, wind speed and direction prescribed at the 24 model atmospheric levels. Sea surface temperature is prescribed by ERA5 reanalysis on a 6-hourly basis. Firn is initialised with a former MARv3.13 10-year spin-up simulation at 10 km spatial resolution using initial snowpack densities of 500 kg m^{-3} and 920 kg m^{-3} above and below the equilibrium line at ~1200 m a.s.l., respectively. Before conducting the 1940-2023 MARv3.14 simulation at 5 km, an additional 4-year spin-up is carried out with snowpack initialisation from the former MARv3.13 run at 10 km. Ice albedo is fixed at 0.55 as a constant in space and time. Surface topography and ice mask are fixed and derived from the 1' resolution digital elevation model ETOPO01[59] and the European Space Agency (ESA) Climate Change Initiative (CCI) Land Cover User Tool version 3.10[60] at 1 km resolution, both down-sampled to 5 km.

Compared to the high-resolution glacier outlines from the Randolph Glacier Inventory version 6 (RGI 6.0)[61], MAR at 5 km generally overestimates ice extent in low-lying ablation areas, notably in SPI (Supplementary Fig. 1a). Surface topography in glacier areas is overall 609 m lower in MAR than in the high resolution Shuttle Radar Topography Mission (SRTM) digital elevation model (DEM)[30] (Supplementary Fig. 2b), with small outlet glaciers being generally too high, and mountain divides and promontories being too low. As a result, glacier hypsometry, i.e., the area-elevation distribution (Supplementary Fig. 9a), is overestimated at low elevations in MAR (green line) relative to SRTM DEM (black line), notably in ablation areas below 1200 m a.s.l., and vice-versa further inland (Supplementary Fig. 9b). Using 74 in-situ SMB measurements for model evaluation, we find that MAR overestimates SMB across low-lying outlet glaciers, and underestimates SMB in inland accumulation zones, where erroneous ablation conditions are captured (Supplementary Fig. 5a). Poor agreement with in-situ observations ($R^2 = 0.05$) and large RMSE (6.1 m w.e) indicate that MAR typically underestimate SMB across Patagonian glaciers and icefields. This is supported by an overall mass loss overestimate when comparing MAR-derived mass change (SMB - D) with GRACE/GRACE-FO records (RMSE = 606 Gt) (green and red lines in Supplementary Fig. 4a).

RACMO: regional atmospheric climate model

The Regional Atmospheric Climate Model version 2.3p2 (RACMO2.3p2) incorporates the dynamical core of the High Resolution Limited Area Model (HIRLAM)[62] and the physics package cycle CY33r1 of the European Centre for Medium-Range Weather Forecasts-Integrated Forecast System (ECMWF-IFS)[63]. The model is specifically adapted to represent surface processes of polar ice sheets and ice caps, including the Greenland ice sheet[26], Canadian Arctic[64], Svalbard[65], Iceland[66], Patagonia[17] and Antarctica[67]. The model has a 40-layer snow module simulating melt, percolation and retention into firn and subsequent surface runoff[68]. The model represents dry-snow densification[69], drifting snow erosion[70], and snow albedo based on grain size, cloud optical thickness, solar zenith angle, and impurity content[71]. RACMO2.3p2 at 5.5 km spatial resolution is forced by ERA5 reanalysis[27] (1979–2023) within a 24-grid-cell-wide relaxation zone at the lateral model boundaries. Forcing consists of temperature, pressure, specific humidity, wind speed and direction being prescribed at the 40 model atmospheric levels every 3 hours. Upper atmospheric

relaxation is active[72]. Sea surface temperature is prescribed from the ERA5 reanalysis on a 3-hourly basis. Firn is initialised on 1st January 1979 by prescribing an initial snow depth (4 m), temperature (−10 °C), and density profile (300–900 kg m^{-3}), followed by a 5-year spin-up simulation (1979-1983). The spin-up ensures that the snowpack properties reach equilibrium with atmospheric conditions. The presented 1979–2023 simulation is then branched from the 5-year spin-up. Ice albedo is prescribed as a constant field in space and time at 0.55. Surface topography and ice mask are fixed and derived from the 30" resolution digital elevation model GTOPO30[73] and the Global Land Cover Characteristics[63] at 1 km resolution, both down-sampled to 5.5 km.

RACMO at 5.5 km spatial resolution resolves the three major ice-fields relatively well (Supplementary Fig. 1a), but does not capture the smaller neighbouring mountain glaciers outlined in the high-resolution RGI 6.0 product[61]. Relative to the SRTM DEM[30], RACMO shows patterns of surface elevation bias similar to those of MAR, though being smaller on average (529 m) (Supplementary Fig. 2c). As opposed to MAR, glacier hypsometry in RACMO at 5.5 km is underestimated below 600 m a.s.l. (Supplementary Fig. 9d), as low-lying glaciers are generally not captured. This is supported by model evaluation using 74 in-situ measurements (Supplementary Fig. 5c), showing an overall SMB overestimate in the ablation zone. RACMO aligns better with in-situ observations ($R^2 = 0.55$) than MAR ($R^2 = 0.05$), although with similar RMSE (6.3 m w.e.) and an over three-fold larger positive bias (3 m w.e.). Comparison to GRACE/GRACE-FO mass loss records confirms a SMB overestimate in RACMO, with an erroneous and persistent mass gain since 2002 (blue line in Supplementary Fig. 4a), in line with previous studies[17,20]. In addition, RACMO-derived mass change RMSE (1227 Gt) is two-fold larger than that of MAR (606 Gt) (Supplementary Fig. 4a).

Statistical downscaling

MAR (1940-2023) and RACMO (1979–2023) SMB components are statistically downscaled from the native model resolution of 5 km and 5.5 km, respectively, to a 500 m ice mask and topography derived from RGI 6.0 (1950–2010)[61] and the high-resolution SRTM DEM version 4 (2000)[30]. The downscaling procedure corrects individual SMB components for elevation on the 500 m topography, using daily-specific vertical gradients estimated on the native model grids. SMB components (X in Eq. (1)) include total precipitation (PR), total sublimation (SU), total melt (ME), and runoff (RU). Drifting snow erosion (ER) is accounted for in RACMO. Vertical gradients are estimated as linear regressions using at least six grid-cells, i.e., the current one and at least five (up to eight) adjacent pixels. To obtain realistic local estimates, the regression slope (a) is applied to the current grid-cell to compute an intercept (b), i.e., value at sea level. These two regression coefficients are bi-linearly interpolated from the low-resolution model grids onto the high resolution one, and applied to the SRTM DEM surface topography at 500 m (h) as,

$$X_{500m} = a_{500m} \times h_{500m} + b_{500m} \tag{1}$$

Melt and runoff are further corrected for surface albedo in regions exposing dark bare ice (albedo < 0.55) in summer, which are unresolved in MAR and RACMO. To that end, we use a 500 m MODIS 16-day product averaged for the period 2000–2023. MODIS bare ice albedo is estimated as the mean of the 5% lowest surface albedo recorded each year, averaged for the period 2000-2023. In addition, daily snowfall fraction (SF$_{frac}$), i.e., the fraction of snowfall on total precipitation, is statistically downscaled to 500 m following Huai et al. (2022)[74]. Snowfall is thus estimated as,

$$SF_{500m} = PR_{500m} \times SF_{frac500m} \tag{2}$$

Rainfall is estimated as a residual as,

$$RA_{500m} = PR_{500m} - SF_{500m} \qquad (3)$$

SMB is reconstructed using individual components statistically downscaled to 500 m as,

$$SMB_{500m} = PR_{500m} - RU_{500m} - SU_{500m} - ER_{500m} \qquad (4)$$

Note that the drifting snow erosion flux (ER) is not accounted for in MAR. Refreezing (RF) is estimated as a residual following,

$$RF_{500m} = ME_{500m} + RA_{500m} - RU_{500m} \qquad (5)$$

Spatial refinement and adjustment

In MAR, statistical downscaling results in a 6% increase in total precipitation (9.4 Gt yr^{-1} for 1940-2023) combined with a 19% decrease in surface runoff (39.4 Gt yr^{-1}), in turn enhancing SMB by 48.0 Gt yr^{-1} (Supplementary Table 1). Total precipitation mostly increases around the hypsometry peak of Patagonian glaciers situated between 1000-1600 m a.s.l. (Supplementary Fig. 9a–c), where MAR at 5 km substantially underestimates surface elevation and glacier area. This is in excellent agreement with PMET-derived vertical precipitation profile (cyan line in Supplementary Fig. 9c). Surface runoff decreases below the hypsometry peak, where MAR at 5 km largely overestimates glacier area, and increases to a smaller extent inland above the hypsometry peak, where glacier area is underestimated (Supplementary Fig. 9a–c). Compared to in-situ SMB records, statistical downscaling significantly improves upon the native MAR product at 5 km, with higher correlation (R^2 = 0.83) and essentially halved RMSE (3.3 m w.e.) (Supplementary Fig. 5a–b). Statistical downscaling also improves MAR-derived mass change agreement with GRACE/GRACE-FO, i.e., the RMSE is almost eliminated (36 Gt) and reduced by 94% relative to the native product at 5 km (green lines in Supplementary Fig. 4a, b). In view of the good agreement with in-situ measurements, PMET precipitation accumulation, and GRACE/GRACE-FO mass change, we deem that no further adjustment is required for downscaled MAR.

In RACMO, runoff increases by 92% (79.7 Gt yr^{-1} for 1979-2023) through statistical downscaling. This is almost balanced by a 40% increase in total precipitation (72.3 Gt yr^{-1}), hence only reducing SMB by 7% (6.8 Gt yr^{-1}) relative to the native product at 5.5 km. RACMO generally underestimates glacier area at all elevations (Supplementary Fig. 9d), notably below and around the Patagonian glacier hypsometry peak (1000-1600 m a.s.l.). The largest increases in total precipitation and runoff are thus found in low-lying (respectively elevated) regions where outlet (respectively mountain) glaciers were not resolved at 5.5 km (Supplementary Fig. 9d, e). As mentioned in previous studies[17,20], RACMO at 5.5 km exaggerates orographic-forced precipitation across the Andes. This process is amplified through statistical downscaling as demonstrated by large precipitation overestimates relative to the PMET data set (cyan line in Supplementary Fig. 9f). This is supported by large SMB overestimate compared to in-situ measurements in the accumulation zone (Supplementary Fig. 5d). Nonetheless, we find that statistical downscaling improves upon the native product at 5.5 km, with higher correlation (R^2 = 0.79) and lower RMSE (5.3 m w.e.) (Supplementary Fig. 5c, d). Comparing downscaled RACMO-derived mass change with GRACE/GRACE-FO shows similar positive bias, correlation and RMSE to the native product at 5.5 km (Supplementary Fig. 4a, b), the result of almost unchanged SMB as precipitation increase compensates for enhanced runoff. In line with remote sensing, the amplitude of seasonal mass change has increased, i.e., with higher winter accumulation and summertime ablation. Reducing total precipitation by 36.5% (92.0 Gt yr^{-1} in Supplementary Table 1) across all glacier grid-cells on a daily basis eliminates the remaining positive bias and

decreases mass change RMSE to 31 Gt relative to remote sensing (blue line in Supplementary Fig. 4c). Adjusted precipitation also results in improved vertical profile agreement between downscaled RACMO and PMET products (cyan line in Supplementary Fig. 9g), better aligns with glacier-integrated MAR and PMET precipitation estimates (Supplementary Fig. 7a), and further decreases the SMB RMSE to 4.9 m w.e. compared to in-situ records (Supplementary Fig. 5e).

Spatial integration

To estimate mass fluxes in Gt, we spatially integrate SMB and its individual components over ice-covered grid-cells. To that end, we use RGI 6.0[61] glacier outlines to derive a fractional ice mask with grid-cell values ranging from 0 (ice-free) to 1 (fully ice-covered). The use of a fractional mask (0 to 1 in Supplementary Fig. 10a) instead of a binary one (0 or 1 in Supplementary Fig. 10b) ensures that large glacier area overestimate is prevented, notably for small mountain glaciers covering less than 0.25 km^2 (i.e., area of a 500 m grid-cell). Here, we estimate glacier-integrated SMB and individual components (M in Gt) as,

$$M = \sum m_{i,j} \times A_{i,j} \times I_{i,j} \times 1e^{-6} \qquad (6)$$

where $m_{i,j}$ is the SMB (or individual components) expressed in kg m^{-2} (or mm w.e.) and estimated for grid-cell i,j; $A_{i,j}$ is the area of grid-cell i,j set to 0.25 km^2; $I_{i,j}$ is the fractional ice mask of grid-cell i,j.

Uncertainty estimates

For glacier-integrated SMB (components), uncertainties are estimated as the annual model difference (MAR minus RACMO) in glacier-integrated SMB (components), statistically downscaled to 500 m and averaged for the overlapping period 1979–2023. Here RACMO estimates include the adjustment in total precipitation (-36.5%). These uncertainties are shown in Supplementary Fig. 6 (Diff) and listed in Supplementary Table 1 (Difference).

For glacier mass change (MB = SMB - D), we sum the uncertainty in D estimated at 1.7 Gt yr^{-1} in Minowa et al. (2021)[12], with that of SMB estimated as the RMSE of the model difference (MAR minus RACMO; 7.3 Gt yr^{-1} in Supplementary Fig. 6a), further halved to 3.7 Gt yr^{-1} to yield an equally distributed positive and negative uncertainty around our SMB estimates. We thus obtain a model mass change uncertainty of 5.4 Gt yr^{-1} as listed in Supplementary Table 2. For cumulative mass change and contribution to sea-level rise, we cumulate monthly mass change uncertainty in time (0.45 Gt per month), from January 1940 to December 2023 (Fig. 1a). Sea-level rise uncertainties are derived from the latter monthly cumulative mass change uncertainties, assuming that 362.5 Gt of ice raises global sea level by 1 mm, as in Cogley et al. (2011)[75].

Product strengths and limitations

The SMB of Patagonian icefields was previously estimated on a 450 m grid[13,18,19]. In contrast to the current study, these previous SMB estimates i) were temporally limited to 1975-2015 (41 years), ii) spatially restricted to NPI and SPI icefields, relied on non-polar regional climate models that iii) were forced by former, low-resolution climate reanalyses including NCEP-NCAR (~ 250 km) and ERA-Interim (~75 km), and iv) do not capture snow processes such as rain and meltwater retention/refreezing in firn, and subsequent runoff. In addition, these studies assumed spatially and temporally fixed lapse rates to statistically downscale modelled meteorological data to 450 m, including precipitation, temperature and solar radiation. These data at 450 m are then used to force simplified mass balance models that derive accumulation from downscaled precipitation (i.e., neglecting condensation/sublimation), and simulate ablation using downscaled temperature, solar radiation and prescribed snow and ice albedo (i.e., neglecting rain and melt retention in firn). In contrast, MAR and

RACMO are forced by the latest ERA5 reanalysis (31 km), quantify melt by solving the full glacier surface energy budget, i.e., including both radiative and turbulent fluxes, and simulate the albedo of snow, firn retention processes and runoff using multi-layer snow modules. Individual modelled SMB components are further statistically downscaled to 500 m using local (spatially varying), daily specific gradients. In addition, we use MODIS satellite records at 500 m to correct downscaled melt and runoff fluxes for the albedo of dark bare ice exposed in summer across ablation zone areas. The resulting statistically downscaled products were thoroughly evaluated using a comprehensive set of independent observations, including i) averaged solid ice discharge estimates for 1968–1999[1] and 2000–2019[12], ii) previously published geodetic, glaciological and remote sensing mass change measurements, complemented with GRACE/GRACE-FO records and the latest GlaMBIE assessment[8] (Supplementary Table 2), iii) point in-situ measurements spanning the three main icefields over the period 1980–2019 (Supplementary Fig. 5), iv) gridded precipitation and temperature observations from two meteorological products CR2MET (1960–2021)[32] and PMET (1980–2020)[31] (Supplementary Fig. 7). Such detailed evaluation has never been achieved in the literature and yielded generally good model agreement, demonstrating the robustness and strength of our statistical downscaling approach and associated high-resolution products.

Patagonian glaciers and icefields have been retreating since the Little Ice Age, with a glacier extent reduction of roughly 2200 km² between 1986 and 2016[76]. However, our two regional climate models and statistical downscaling approach do not account for ice dynamics processes driving glacier retreat and thinning. Instead, we use fixed surface elevation and glacier extent from the SRTM DEM version 4 (2000)[30] and RGI 6.0 (1950-2010)[61], yielding conservative present-day SMB estimates. However, glacier retreat can affect the spatial distribution of SMB components, notably in marginal ablation zones. For instance, area-integrated meltwater runoff may decrease as ablation zone extent shrinks. In contrast, glacier thinning may trigger pronounced melt-elevation feedback, i.e., enhanced meltwater runoff rates as temperature increases with surface lowering. Quantifying these competing mechanisms requires coupling regional climate models to a dedicated ice dynamics module, as was previously done for the Greenland ice sheet[77]. To date, such coupling has never been achieved for the small Patagonian glaciers and icefields. As an alternative, we explored the response of SMB components to glacier retreat by quantifying the difference obtained when spatially integrating downscaled MAR SMB components over the reduced glacier extent of the latest RGI version 7 (RGI 7.0, 1950–2021)[78]. Relative to RGI 6.0 (1950–2010), glacier area in RGI 7.0 declines by roughly 1500 km². We find that using the RGI 7.0 ice mask, glacier-integrated total precipitation and runoff decrease by 3.7 Gt yr⁻¹ (2.2%) and 13.0 Gt yr⁻¹ (8.0%) on average for 1940–2023, hence resulting in a 6.4 Gt yr⁻¹ SMB increase. These changes are insignificant as they remain lower than one SD of the long-term SMB components averages (1940-2023; Supplementary Fig. 11), i.e., SD = 15.2 Gt yr⁻¹, 21.1 Gt yr⁻¹, and 25.7 Gt yr⁻¹ for total precipitation, runoff and SMB, respectively. Note that these changes do not account for melt-elevation feedback resulting from associated glacier thinning, which could significantly increase surface runoff.

Data availability

Annual SMB (and components) data sets from MARv3.14 (1940-2023) and (adjusted) RACMO2.3p2 (1979-2023) at 500 m have been deposited on Zenodo [https://zenodo.org/records/13768195][79]. Larger files, including the gridded, daily downscaled SMB (components) data sets from MARv3.14 and RACMO2.3p2 simulations, are freely available from the authors upon request and without conditions (bnoel@uliege.be).

Code availability

The statistical downscaling technique is presented in Noël et al. (2016, 2023)[28,29].

References

1. Rignot, E., Rivera, A. & Casassa, G. Contribution of the patagonia icefields of south america to sea level rise. *Science* **302**, 434–437 (2003).
2. Farinotti, D. et al. A consensus estimate for the ice thickness distribution of all glaciers on Earth. *Nat. Geosci.* **12**, 168–173 (2019).
3. Millan, R. et al. Ice thickness and bed elevation of the northern and southern patagonian icefields. *Geophys. Res. Lett.* **46**, 6626–6635 (2019).
4. Rivera, A., Benham, T., Casassa, G., Bamber, J. & Dowdeswell, J. Ice elevation and areal changes of glaciers from the northern patagonia icefield, chile. *Glob. Planet. Change* **59**, 126–137 (2007).
5. Aniya, M. Holocene variations of ameghino glacier, southern patagonia. *Holocene* **6**, 247–252 (1996).
6. Angelis, H. D. Hypsometry and sensitivity of the mass balance to changes in equilibrium-line altitude: the case of the southern patagonia icefield. *J. Glaciol.* **60**, 14–28 (2014).
7. Bown, F., Rivera, A., Zenteno, P., Bravo, C. & Cawkwell, F. *First Glacier Inventory and Recent Glacier Variation on Isla Grande de Tierra Del Fuego and Adjacent Islands in Southern Chile. In: Global Land Ice Measurements from Space.* (Springer Praxis Books, 2014).
8. The GlaMBIE Team. Community estimate of global glacier mass changes from 2000 to 2023. *Nature* 1–23 (2025).
9. Zemp, M. et al. Global glacier mass changes and their contributions to sea-level rise from 1961 to 2016. *Nature* **568**, 382–386 (2019).
10. Braun, M. H. et al. Constraining glacier elevation and mass changes in South America. *Nat. Clim. Change* **9**, 130–136 (2019).
11. Bamber, J. L., Westaway, R. M., Marzeion, B. & Wouters, B. The land ice contribution to sea level during the satellite era. *Environ. Res. Lett.* **13**, 063008 (2018).
12. Minowa, M., Schaefer, M., Sugiyama, S., Sakakibara, D. & Skvarca, P. Frontal ablation and mass loss of the patagonian icefields. *Earth Planet. Sci. Lett.* **561**, 116811 (2021).
13. Carrasco-Escaff, T., Rojas, M., Garreaud, R. D., Bozkurt, D. & Schaefer, M. Climatic control of the surface mass balance of the patagonian icefields. *Cryosphere* **17**, 1127–1149 (2023).
14. Hock, R. et al. GlacierMIP - A model intercomparison of global-scale glacier mass-balance models and projections. *J. Glaciol.* **65**, 453–467 (2019).
15. Bravo, C., Bozkurt, D., Ross, A. N. & Quincey, D. J. Projected increases in surface melt and ice loss for the northern and southern patagonian icefields. *Nat. Sci. Rep.* **11**, 1–13 (2021).
16. Mernild, S. H., Liston, G. E., Hiemstrad, C. & Wilsone, R. The andes cordillera. part III: Glacier surface mass balance and contribution to sea level rise (1979-2014). *Int. J. Climatol.* **37**, 3154–3174 (2017).
17. Lenaerts, J. T. M. et al. Extreme precipitation and climate gradients in patagonia revealed by high-resolution regional atmospheric climate modeling. *J. Clim.* **27**, 4607–4621 (2014).
18. Schaefer, M., Machguth, H., Falvey, M. & Casassa, G. Modeling past and future surface mass balance of the northern patagonia icefield. *J. Geophys. Res.: Earth Surf.* **118**, 571–588 (2013).
19. Schaefer, M., Machguth, H., Falvey, M., Casassa, G. & Rignot, E. Quantifying mass balance processes on the southern patagonia icefield. *Cryosphere* **9**, 25–35 (2015).
20. Sauter, T. Revisiting extreme precipitation amounts over southern south america and implications for the patagonian icefields. *Hydrol. Earth Syst. Sci.* **24**, 2003–2016 (2020).
21. Foresta, L. et al. Heterogeneous and rapid ice loss over the patagonian ice fields revealed by cryosat-2 swath radar altimetry. *Remote Sens. Environ.* **211**, 441–455 (2018).

22. Malz, P. et al. Elevation and mass changes of the southern patagonia icefield derived from TanDEM-X and SRTM Data. *Remote Sens.* **10**, 1–17 (2018).

23. Dussaillant, I. et al. Two decades of glacier mass loss along the andes. *Nat. Geosci.* **12**, 802–808 (2019).

24. Wouters, B., Gardner, A. S. & Moholdt, G. Global glacier mass loss during the GRACE satellite mission (2002-2016). *Front. Earth Sci.* **7**, 1–11 (2019).

25. Hugonnet, R. et al. Accelerated global glacier mass loss in the early twenty-first century. *Nature* **592**, 726–731 (2021).

26. Noël, B., van de Berg, W. J., Lhermitte, S. & van den Broeke, M. R. Rapid ablation zone expansion amplifies north greenland mass loss. *Sci. Adv.* **5**, eaaw0123 (2019).

27. Hersbach, H. et al. The ERA5 global reanalysis. *Q. J. R. Meteor-ological Soc.* **146**, 1999 – 2049 (2020).

28. Noël, B. et al. A daily, 1 km resolution data set of downscaled greenland ice sheet surface mass balance (1958-2015). *Cryosphere* **10**, 2361 – 2377 (2016).

29. Noël, B. et al. Higher Antarctic ice sheet accumulation and surface melt rates revealed at 2 km resolution. *Nat. Commun.* **14**, 1–11 (2023).

30. Farr, T. G. et al. The shuttle radar topography mission. *Rev. Geo-phys.* **45**, 1–33 (2007).

31. Aguayo, R. et al. PatagoniaMet: a multi-source hydrometeorological dataset for western patagonia. *Sci. data* **11**, 1 – 15 (2024).

32. Boisier, J. P. & Alvarez-Garreton, C. CR2MET: A high-resolution precipitation and temperature dataset for the period 1960-2021 in continental Chile. *Data set Zenodo* **v2.5**, https://zenodo.org/records/7529682 (2023).

33. Yang, H. et al. Poleward shift of the major ocean gyres detected in a warming climate. *Geophys. Res. Lett.* **47**, e2019GL085868 (2020).

34. Yang, H., Lu, J., Wang, Q., Shi, X. & Lohmann, G. Decoding the dynamics of poleward shifting climate zones using aqua-planet model simulations. *Clim. Dyn.* **58**, 3513–3526 (2022).

35. Roemmich, D. et al. Decadal spinup of the south pacific subtropical gyre. *J. Phys. Oceanogr.* **37**, 162–173 (2007).

36. Roemmich, D., Gilson, J., Sutton, P. & Zilberman, N. Multidecadal change of the south pacific gyre circulation. *J. Phys. Oceanogr.* **46**, 1871–1883 (2016).

37. Yamada, T. Glaciological characteristics revealed by 37.6-m deep core drilled at the accumulation area of san rafael glacier, the northern patagonia icefield. *Bull. Glacier Res.* **4**, 59–67 (1987).

38. Matsuoka, K. & Naruse, R. Mass balance features derived from a firn core at hielo patagónico norte, south america. *Arct., Antarct., Alp. Res.* **31**, 333–340 (1999).

39. Aristarain, A. J. & Delmas, R. J. Firn-core study from the southern patagonia ice cap, south America. *J. Glaciol.* **39**, 249–254 (1993).

40. Rivera, A. *Investigations on Mass Balance and Dynamics of Moreno Glacier based on Field Measurements and Satellite Imagery. Ph.D. dissertation* (Leopold-Franzens-Universitat Innsbruck, 1999).

41. Stuefer, M., Rott, H. & Skvarca, P. Glaciar perito moreno, patagonia: climate sensitivities and glacier characteristics preceding the 2003/04 and 2005/06 damming events. *J. Glaciol.* **53**, 3–16 (2007).

42. Popovnin, V. V., Danilova, T. A. & Petrakov, D. A. A pioneer mass balance estimate for a patagonian glacier: glaciar de los tres, argentina. *Glob. Planet. Change* **22**, 255–267 (1999).

43. Rivera, A. *Mass balance investigations at Glaciar Chico, Southern Patagonia Icefield, Chile. Ph.D. thesis* (University of Bristol, 2004).

44. Schwikowski, M., Brütsch, S., Saurer, M., Casassa, G. & Rivera, A. First shallow firn core record from Gorra Blanca, Patagonia. *Geophys. Res. Abstr.* **5** (2003).

45. Schwikowski, M., Schläppi, M., Santibañez, P., Rivera, A. & Casassa, G. Net accumulation rates derived from ice core stable isotope records of Pío XI glacier, Southern Patagonia Icefield. *Cryosphere* **7**, 1635–1644 (2013).

46. Shiraiwa, T. et al. High net accumulation rates at campo de hielo patagonico sur, south america, revealed by analysis of a 45.97 m long ice core. *Ann. Glaciol.* **35**, 84–90 (2002).

47. Temme, F. et al. Strategies for regional modeling of surface mass balance at the monte sarmiento massif, tierra del fuego. *Cryosphere* **17**, 2343–2365 (2023).

48. Haakensen, N. Glacier mapping to confirm results from mass-balance measurements. *Ann. Glaciol.* **8**, 73–77 (1986).

49. Midgley, N. & Tonkin, T. Reconstruction of former glacier surface topography from archive oblique aerial images. *Geomorphology* **282**, 18–26 (2017).

50. Gallée, H. & Schayes, G. Development of a three-dimensional meso-γ primitive equation model: katabatic winds simulation in the area of terra nova bay, antarctica. *Monthly Weather Rev.* **122**, 671–685 (1994).

51. Fettweis, X., Gallée, H., Lefebre, F. & van Ypersele, J.-P. Greenland surface mass balance simulated by a regional climate model and comparison with satellite-derived data in 1990-1991. *Clim. Dyn.* **24**, 623–640 (2005).

52. Delhasse, A. et al. Brief communication: Evaluation of the near-surface climate in ERA5 over the greenland ice sheet. *Cryosphere* **14**, 957–965 (2020).

53. Maure, D., Kittel, C., Lambin, C., Delhasse, A. & Fettweis, X. Spatially heterogeneous effect of climate warming on the arctic land ice. *Cryosphere* **17**, 4645–4659 (2023).

54. Kittel, C. et al. Diverging future surface mass balance between the antarctic ice shelves and grounded ice sheet. *Cryosphere* **15**, 1215 – 1236 (2021).

55. Ridder, K. D. & Schayes, G. The IAGL land surface model. *J. Appl. Meteorol. Climatol.* **36**, 167–182 (1997).

56. Gallée, H., Guyomarc'h, G. & Brun, E. Impact of snow drift on the antarctic ice sheet surface mass balance: Possible sensitivity to snow-surface properties. *Bound.-Layer. Meteorol.* **99**, 1–19 (2001).

57. Lefebre, F., Gallée, H., van Ypersele, J.-P. & Greuell, W. Modeling of snow and ice melt at ETH camp (West Greenland): A study of surface albedo. *J. Geophys. Res. Lett. Atmospheres* **108**, 4231 (2003).

58. Brun, E., Martin, E., Simon, V., Gendre, C. & Coleou, C. An energy and mass model of snow cover suitable for operational avalanche forecasting. *J. Glaciol.* **35**, 333–342 (1989).

59. Amante, C. & Eakins, B. W. *ETOPO1 1 Arc-Minute Global Relief Model: Procedures, Data Sources and Analysis* (NOAA Technical Memor-andum NESDIS NGDC-24. National Geophysical Data Center, NOAA, 2009). https://www.ngdc.noaa.gov/mgg/global/relief/ETOPO1/docs/ETOPO1.pdf.

60. Defourny, P. et al. *Land Cover CCI Product User Guide Version 2: Technical Report* (ESA, 2017).

61. RGI 6.0 Consortium. *Randolph Glacier Inventory-A Dataset of Global Glacier Outlines: Version 6.0: Technical Report* (Global Land Ice Measurements from Space, 2017). https://doi.org/10.7265/N5-RGI-60.

62. Undén, P. et al. *HIRLAM-5: Scientific Documentation* (HIRLAM-5 Project, Norrköping, Sweden, 2002).

63. ECMWF. *IFS Documentation CY33R1, Part IV : PHYSICAL PRO-CESSES (CY33R1)* (ECMWF, Reading, UK, 2009).

64. Noël, B. et al. Six decades of glacial mass loss in the canadian arctic archipelago. *J. Geophys. Res.-Earth Surf.* **123**, 1430–1449 (2018).

65. Noël, B. et al. Low elevation of svalbard glaciers drives high mass loss variability. *Nat. Commun.* **11**, 8 (2020).

66. Noël, B. et al. North atlantic cooling is slowing down mass loss of icelandic glaciers. *Geophys. Res. Lett.* **49**, e2021GL095697 (2022).

67. van Wessem, J. et al. Modelling the climate and surface mass bal-ance of polar ice sheets using RACMO2 - Part 2: Antarctica (1979-2016). *Cryosphere* **12**, 1479 – 1498 (2018).

68. Ettema, J. et al. Climate of the greenland ice sheet using a high-resolution climate model - Part 1: Evaluation. *Cryosphere* **4**, 511 – 527 (2010).

69. Ligtenberg, S., Helsen, M. M. & van den Broeke, M. R. An improved semi-empirical model for the densification of antarctic firn. *Cryosphere* **5**, 809 – 819 (2011).

70. Lenaerts, J., van den Broeke, M. R., Angelen, J. H., van Meijgaard, E. & Déry, S. J. Drifting snow climate of the greenland ice sheet: a study with a regional climate model. *Cryosphere* **6**, 891 – 899 (2012).

71. Kuipers Munneke, P. et al. A new albedo parameterization for use in climate models over the Antarctic ice sheet. *J. Geophys. Res.* **116**, D05114 (2011).

72. van de Berg, W. & Medley, B. Brief communication: Upper-air relaxation in RACMO2 significantly improves modelled interannual surface mass balance variability in antarctica. *Cryosphere* **10**, 459 – 463 (2016).

73. Gesch, D. B., Verdin, K. L. & Greenlee, S. K. New land surface digital elevation model covers the earth. *Eos, Earth Space Sci. N.* **80**, 69–70 (1999).

74. Huai, B., van den Broeke, M., Reijmer, C. & Noël, B. A daily, 1 km resolution Greenland rainfall climatology (1958 2020) from statistical downscaling of a regional atmospheric climate model. *J. Geophys. Res. Atmospheres* **127**, e2022JD036688 (2022).

75. Cogley, J. et al. *Glossary of glacier mass balance and related terms* (UNESCO-IHP, IHP-VII Technical documents in hydrology 86, IACS contribution 2, 2011). http://unesdoc.unesco.org/images/0019/001925/192525E.pdf.

76. Meier, W. J.-H., Grießinger, J., Hochreuther, P. & Braun, M. H. An updated multi-temporal glacier inventory for the patagonian andes with changes between the little ice age and 2016. *Front. Earth Sci.* **6**, 1–21 (2018).

77. Delhasse, A., Beckmann, J., Kittel, C. & Fettweis, X. Coupling MAR (modèle atmosphérique régional) with PISM (parallel ice sheet model) mitigates the positive melt-elevation feedback. *Cryosphere* **18**, 633–651 (2024).

78. RGI 7.0 Consortium. *Randolph Glacier Inventory - A Dataset of Global Glacier Outlines, Version 7.0* (NSIDC: National Snow and Ice Data Center, Boulder,Colorado USA, 2023). https://doi.org/10.5067/f6jmovy5navz.

79. Noël, B. et al. Data set: "Poleward shift of subtropical highs drives Patagonian glacier mass loss". *Zenodo [Data set]* https://zenodo.org/records/13768195.

Acknowledgements

Author contributions

B.N. designed the study, prepared the manuscript, conducted the RAC-MO2.3p2 simulations at 5.5 km, and statistically downscaled the two presented data sets to 500 m. X.F. conducted the MARv3.14 simulations at 5 km. B.W. provided mass change records from GRACE/GRACE-FO. S.L. helped to prepare the MODIS albedo time series. B.N., S.L., B.W. and X.F. commented on the manuscript.

Competing interests

The authors declare no competing interests.

Additional information

Supplementary information The online version contains supplementary material available at https://doi.org/10.1038/s41467-025-58974-1.

Correspondence and requests for materials should be addressed to Brice Noël.

Peer review information *Nature Communications* thanks Andres Rivera and the other, anonymous, reviewer(s) for their contribution to the peer review of this work. A peer review file is available.

Reprints and permissions information is available at http://www.nature.com/reprints

Publisher's note Springer Nature remains neutral with regard to jurisdictional claims in published maps and institutional affiliations.